Optimal Design of a Hybrid Wireless Power Transfer System With High Voltage Gain and High Efficiency

Ting Chen, *Member, IEEE*, Yuqiao Wang, Fengxian Wang, Xian Zhang, Xuan Zhao, Guangyao Li,
and Zhihui Ma

***Abstract*—This article presents a novel hybrid wireless power transfer system that achieves both high voltage gain and high efficiency through an integrated dual-mode power transfer mechanism. The proposed system employs a compact hybrid coupler composed of two pairs of decoupled bipolar coils at the center and two pairs of decoupled transmitter–receiver capacitive plates surrounding the coils. This unique configuration establishes two independent electric-field power transfer channels and two independent magnetic-field channels, effectively suppressing cross-coupling between adjacent channels and enabling simultaneous multichannel power transmission. To regulate power distribution between the inductive and capacitive paths, an S-SP compensation network is adopted, featuring asymmetrical external capacitors on the primary and secondary sides. This compensation strategy facilitates constant voltage output while enhancing voltage gain and overall system efficiency. Comprehensive theoretical analysis is conducted to investigate the influence of coupler geometry and compensation parameters on system gain. A two-channel experimental prototype is developed to validate the proposed system architecture. Experimental results demonstrate a 140% gain range extension, with a maximum dc–dc efficiency of 86%.**

***Index Terms*—Constant voltage outputs, high voltage gain, hybrid wireless power transfer, integrated coupler.**

I. INTRODUCTION

WIRELESS power transfer (WPT) is an emerging technology that achieves contactless power delivery through spatial electromagnetic conversion [1], [2]. It has been gaining popularity in applications ranging from consumer electronics to electric vehicles and biomedical implants due to its advantages of high security, high reliability, and high flexibility [3], [4], [5]. According to the power transfer channel, WPT technologies can be categorized into three types: 1) electric-field coupling, 2) magnetic-field coupling, and 3) highly integrated hybrid wireless power transfer (HWPT) systems [6], [7], [8], [9]. Among these, HWPT systems have emerged as a research focus due to their comprehensive potential for output optimization and enhanced degrees of freedom. Wang et al. [10] introduced an electric field transmission channel into an inductive power transfer (IPT) system to compensate for performance degradation under misalignment, thereby enhancing system robustness. In [11], a HWPT system was proposed in which the compensation inductors of the CPT network formed an additional inductive path, enabling more efficient component utilization. Li et al. [12] proposed a modeling method for hybrid resonators based on dual single-layer PCB structures. In related work, Li et al. [13] proposed a novel comb-shaped coupler structure that achieves compact integration of inductive and capacitive coupling paths, effectively improving space utilization. These studies demonstrate the diverse design goals pursued in HWPT research and highlight the potential of hybrid systems for integration.

As research continues to advance, application scenarios have expanded from specific domains to more diverse and complex environments. Different devices and contexts often require widely varying input voltage levels. As a result, wide-range voltage gain has evolved to a core performance metric that determines the interoperability and practical viability of WPT systems [14], [15]. One critical factor in enabling wide voltage gain tuning is overcoming the inherent limitations imposed by coil parameters [16]. To address this, various strategies have been developed to extend the achievable voltage gain range. One approach is to employ high-order compensation networks [17], [18]. In conventional series- or parallel-compensated networks, voltage gain is highly dependent on the coupling coefficient, making wide-range adjustment difficult. In contrast, high-order networks address this issue by introducing additional resonant components (e.g., multiple *LC* stages in series or parallel), thereby improving gain tuning flexibility and enhancing system efficiency [19], [20]. However, the inclusion of extra inductive

Received 24 June 2025; revised 3 September 2025; accepted 19 September 2025. Date of publication 25 September 2025; date of current version 23 December 2025. This work was supported in part by the National Natural Science Foundation of China under Grant 52307009, in part by Hebei Province Yan Zhao Golden Terrace Talent Gathering Plan Key Talent Project under Grant B2024011, in part by the State Key Laboratory of Reliability and Intelligence of Electrical Equipment under Grant EERI_OY2023001, in part by the National Natural Science Foundation of China under Grant 52122701 and Grant 52477005, in part by the Key Program of Natural Science Foundation of Tianjin under Grant 22JCZDJC00620, in part by the Hebei Provincial Central Guidance Local Science and Technology Development Project under Grant 236Z5201G, in part by the Hebei Yanzhao Young Scientist Project under Grant E2024202109, in part by the S&T Program of Hebei under Grant 24464401D, and in part by the Continuation Funding Project for Innovative Research Groups of Natural Science Foundation of Hebei Province under Grant E2024202298. Recommended for publication by Associate Editor M. Ponce-Silva. *(Corresponding author: Ting Chen.)*

The authors are with the State Key Laboratory of Intelligent Power Distribution Equipment and System, Hebei University of Technology, Tianjin 300401, Chinaand also with the Hebei Key Laboratory of Equipment and Technology Demonstration of Flexible DC Transmission, Hebei University of Technology, Tianjin 300401, China (e-mail: tingchen@hebut.edu.cn; 202331402008@stu.hebut.edu.cn; 202111401013@stu.hebut.edu.cn; zhangxian@hebut.edu.cn; 202211401015@stu.hebut.edu.cn; 202221401084@stu.hebut.edu.cn; 202321401107@stu.hebut.edu.cn).

Color versions of one or more figures in this article are available at https://doi.org/10.1109/TPEL.2025.3614643.

Digital Object Identifier 10.1109/TPEL.2025.3614643

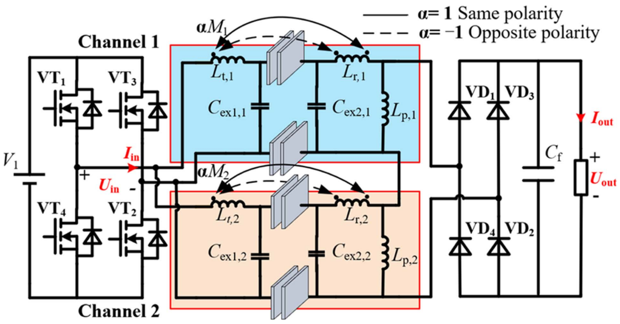

Fig. 1. Proposed circuit of the HWPT system with dual transmitter and dual receiver.

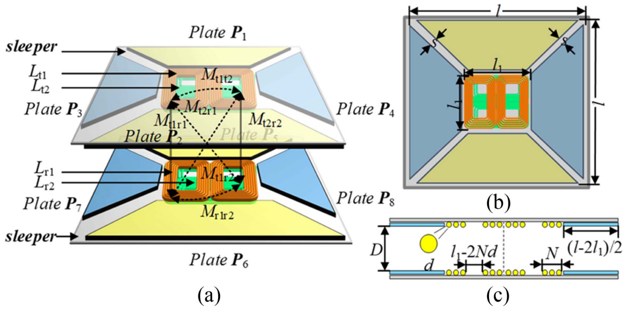

(a) (b) (c)

Fig. 2. Structure and dimensions of the coupler. (a) Three-dimensional view. (b) Top view. (c) Longitudinal section view.

components in high-order compensation networks inevitably increases system volume, cost, and power loss. Another approach is the multichannel cooperative mechanism. Lu et al. [21] and Li et al. [22] developed a single-transmitter multireceiver system based on a cascaded topology, that effectively increased the equivalent turns ratio to achieve a wider voltage range. Liang et al. [23] further proposed a multichannel magnetic coupling system with an input-series output-series (ISOS) structure. By accounting for interchannel coupling effects and introducing a parameter design method to coordinate energy transfer among channels, thus improving the system's voltage regulation capability [23]. Beyond multichannel magnetic coupling approaches, HWPT architectures have also been explored as an alternative means to achieve wide-range gain tuning. Xu et al. [24] proposed a gain variation model for HWPT systems and provided theoretical analysis and comparison of gain characteristics for standalone CPT and IPT, preliminarily demonstrating the advantage of hybrid systems in voltage gain control.

In summary, although extensive research has been conducted on circuit topologies and compensation strategies, the potential of hybrid coupling systems in achieving a wide gain range has not yet been systematically investigated. This article designs a novel hybrid coupler to simultaneously suppress cross-coupling effects of electric and magnetic fields and optimize the spatial layout of coupling coils and metal plates. A gain optimization strategy based on the electric field transmission channel is proposed, in which the roles of the primary and secondary capacitors are decoupled, enabling flexible voltage regulation and supporting high-voltage output. Building upon this foundation, a dual-channel HWPT system is constructed, where each channel integrates an IPT and a CPT channel. By adjusting the electric field transmission path and optimizing the parameters α and β, where α denotes the wiring factor and β represents the power transfer ratio, the system achieves flexible voltage gain regulation, providing a new solution for WPT systems requiring wide-range voltage gain. Compared with previous studies. in this work, α and β are explicitly formulated as optimization variables to represent system power behavior, rather than being merely used as modeling parameters [25], [26].

The rest of this article is organized as follows. Section II presents and describes the proposed system, detailing the decoupling methods for the coupler. Section III analyzes the compensation network and compares it with a single system. Section IV establishes an experimental prototype to prove the validity of the proposed modular HWPT system. Finally, Section V concludes this article. The main contributions of this article are as follows:

1) A novel hybrid coupler is designed to simultaneously suppress cross-coupling effects between electric and magnetic fields while optimizing the spatial arrangement of coupling coils and metal plates. Based on this, an optimization method for the hybrid coupler is proposed by introducing the transmission power ratio β as a design variable, thereby enhancing wide-range voltage gain performance.
2) A dual-channel HWPT system is proposed, in which two decoupled inductive and capacitive transmission paths operate cooperatively. Compared with conventional single-channel systems, the proposed architecture significantly improves the capability of achieving wide-range voltage gain.
3) A compensation network design strategy based on the electric field transmission path is introduced, wherein the functional roles of the primary and secondary external capacitors are decoupled. This enables flexible gain regulation and provides a new solution for efficient wide-range voltage gain control.

II. SYSTEM STRUCTURE AND WORKING PRINCIPLE

A. System Structure

This article proposes a dual-channel cascaded HWPT system based on the multistage voltage boosting technique, as shown in Fig. 1. The system features an input-parallel output-series SP compensation networks. A dc voltage source V_1 supplies high-frequency ac power through a full-bridge inverter. The energy is transferred through the coupler and compensation circuit, and subsequently rectified by a full-bridge diode rectifier to deliver dc power to the load resistor R_{L}.

To enhance power transmission capability, the entire coupler is divided into two decoupled channels. $C_{\mathrm{ex1,1}}$, $C_{\mathrm{ex2,1}}$ and $C_{\mathrm{ex1,2}}$, $C_{\mathrm{ex2,2}}$, are the compensation capacitances. The inductances $L_{\mathrm{p,1}}$ and $L_{\mathrm{p,2}}$ represent the compensation inductance at the secondary side, while $L_{\mathrm{t,1}}$, $L_{\mathrm{r,1}}$, $L_{\mathrm{t,2}}$, and $L_{\mathrm{r,2}}$ are the self-inductances of the coupling coils. Mutual inductance is represented by αM_1 and αM_2, where α is a variable indicating the connection configuration of the coupling coils. When $\alpha = 1$, the coils are connected in series with the coupling plates at the

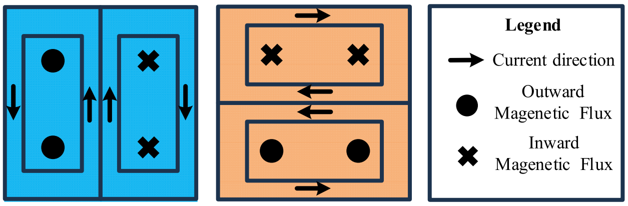

Fig. 3. Coils structure.

same polarity ends. When $\alpha = -1$, the opposite polarity ends of the coils are connected in series with the coupling plates.

The coupling coils and plates act as power channels, with the coils transmitting magnetic field energy and the coupling plates transmitting electric field energy. In this configuration, the coupling inductance and plate capacitance function as complementary compensation components, jointly contributing to power transfer through mutual compensation.

The total series output voltage of the two-channel system U_{out} satisfies

$$U_{\text{out}} = \frac{2\sqrt{2}}{\pi}\left(U_{o,1} + U_{o,2}\right) \tag{1}$$

where $U_{\text{o},1}$ and $U_{\text{o},2}$ are the average ac output voltages of channel 1 and channel 2, respectively.

B. Proposed Magnetic-electric Coupler

Fig. 2 shows the three-dimensional model of the proposed hybrid coupler, which comprises two pairs of decoupled bipolar coils at the center and two decoupled transmitter-receiver plate pairs surrounding them. To reduce eddy current losses, the capacitive plates are placed away from regions of concentrated magnetic flux. This spatial separation suppresses electric–magnetic field interference and preserves the independent resonance of each channel. This configuration establishes two independent electric-field coupling channels and two independent magnetic-field coupling channels, enabling coordinated utilization of both coupling paths and resulting in significant enhancement of voltage gain and overall transmission performance. Decoupling characteristic is the key to achieving efficient multichannel power transfer, as it eliminates interchannel interference and enhances system efficiency and output stability. The detailed decoupling principles and working mechanisms are depicted as follows.

Fig. 3 shows the decoupling principle of inductive coils. To eliminate coupling between adjacent coils, two sets of orthogonal DD coils along different directions are employed in the inductive coupling region. The symmetrical geometry ensures flux cancellation, making the mutual inductance between adjacent coils negligible and forming two orthogonal, decoupled magnetic coupling channels.

From the circuit perspective, the full-capacitor model is too complicated and inconvenient for analysis. To facilitate the analysis of electric field decoupling among multiple plates, an equivalent induced source model is adopted. In the capacitive coupling region, the coupling capacitance between any two capacitive plates P_i and P_j among the eight plates is defined as C_{ij} ($i,j = 12, \ldots, 78$). According to the general capacitance model for multiport electric field coupling structures, the voltage-current relationships among the eight plates can be described by a matrix equation as follows:

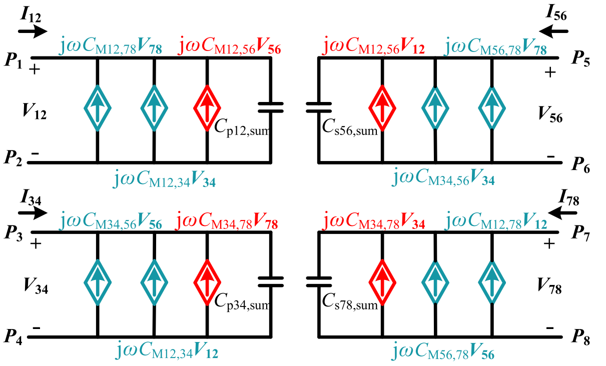

Fig. 4. Plates structure.

$$\begin{bmatrix} \boldsymbol{I_{12}} \\ \boldsymbol{I_{34}} \\ \boldsymbol{I_{56}} \\ \boldsymbol{I_{78}} \end{bmatrix} = \begin{bmatrix} \frac{1}{\text{j}\omega}C^{-1}_{\text{p12,sum}} & -\text{j}\omega C_{\text{M12,34}} & -\text{j}\omega C_{\text{M12,56}} & -\text{j}\omega C_{\text{M12,78}} \\ -\text{j}\omega C_{\text{M12,34}} & \frac{1}{\text{j}\omega}C^{-1}_{\text{p34,sum}} & -\text{j}\omega C_{\text{M34,56}} & -\text{j}\omega C_{\text{M34,78}} \\ -\text{j}\omega C_{\text{M12,56}} & -\text{j}\omega C_{\text{M34,56}} & \frac{1}{\text{j}\omega}C^{-1}_{\text{s56,sum}} & -\text{j}\omega C_{\text{M56,78}} \\ -\text{j}\omega C_{\text{M12,78}} & -\text{j}\omega C_{\text{M34,78}} & -\text{j}\omega C_{\text{M56,78}} & \frac{1}{\text{j}\omega}C^{-1}_{\text{s78,sum}} \end{bmatrix} \begin{bmatrix} \boldsymbol{V_{12}} \\ \boldsymbol{V_{34}} \\ \boldsymbol{V_{56}} \\ \boldsymbol{V_{78}} \end{bmatrix} \tag{2}$$

where $\boldsymbol{V_{12}}$, $\boldsymbol{V_{34}}$, $\boldsymbol{V_{56}}$, and $\boldsymbol{V_{78}}$ are the port voltages, while $\boldsymbol{I_{12}}$, $\boldsymbol{I_{34}}$, $\boldsymbol{I_{56}}$, and $\boldsymbol{I_{78}}$ denote the corresponding port currents. The total capacitance between plates i and j ($i, j = 1, 2, \ldots, 8$) is defined as $C_{\text{p}ij\text{,sum}}$, which represents the sum of the self-capacitances of all two-port networks on the transmission side between plates i and j. The mutual capacitance between plates i, j, and plates m, n ($m, n = 1, 2, \ldots, 7, 8$) is defined as $C_{\text{M}ij,mn}$.

As shown in Fig. 2, geometric symmetry ensures that the distances between plates P_1 and P_3 and between P_1 and P_4 are equal. Similarly, the distance for plates P_2 to P_3 and P_4 are equal, leading to $C_{13} = C_{14}$ and $C_{23} = C_{24}$. According to the multiport mutual capacitance computation method described in [13], it can be derived that $C_{\text{M12,34}} = 0$, achieving decoupling of adjacent plates on the same side. Similarly, since the distances from P_1 and P_2 to P_7 and P_8 are equal, it follows that $C_{\text{M12,78}} = 0$ indicating decoupling between adjacent plates on opposite sides. By symmetry, the mutual capacitances $C_{\text{M34,56}}$ and $C_{\text{M56,78}}$ are zero. As shown in Fig. 4, the matrix equation in (2) of the capacitive plates can be simplified as

$$\begin{gathered} \begin{bmatrix} \boldsymbol{I_{12}} \\ \boldsymbol{I_{56}} \end{bmatrix} = \begin{bmatrix} \frac{1}{\text{j}\omega}C^{-1}_{\text{p12,sum}} & -\text{j}\omega C_{\text{M12,56}} \\ -\text{j}\omega C_{\text{M12,56}} & \frac{1}{\text{j}\omega}C^{-1}_{\text{s56,sum}} \end{bmatrix} \begin{bmatrix} \boldsymbol{V_{12}} \\ \boldsymbol{V_{56}} \end{bmatrix} \\ \begin{bmatrix} \boldsymbol{I_{34}} \\ \boldsymbol{I_{78}} \end{bmatrix} = \begin{bmatrix} \frac{1}{\text{j}\omega}C^{-1}_{\text{p34,sum}} & -\text{j}\omega C^{-1}_{\text{M34,78}} \\ -\text{j}\omega C^{-1}_{\text{M34,78}} & \frac{1}{\text{j}\omega}C^{-1}_{\text{s78,sum}} \end{bmatrix} \begin{bmatrix} \boldsymbol{V_{34}} \\ \boldsymbol{V_{78}} \end{bmatrix}. \end{gathered} \tag{3}$$

TABLE I
SIMULATION PARAMETERS

Parameter	Design value	Note
l	300 mm	Coupler's length
l_1	120 mm	Coil's length
s	5 mm	Plate gap
D	40 mm	Transmission distance
d	2.94 mm	Coil's wire radius

Therefore, in the four-port network formed by the eight plates, plates P_1, P_2, P_5, and P_6 constitute one independent electric field coupling power transfer channel, while plates P_3, P_4, P_7, and P_8 form another.

C. Coupler Parameter Analysis

To quantitatively analyze the parametric effects of the dual-channel coupler, finite element simulations were conducted. In this coupler, both the magnetic field generated by the coils and the electric field generated by the plates exhibit central symmetry. Consequently, the length and width dimensions have the same influence on the electrical parameters of the coupler.

In this section, the Coil's length l_1 is analyzed as a variable to facilitate comparative analysis of the electrical parameter variations with respect to both coupling mechanisms. As shown in Table I, the coupler's length l is set to 300 mm. Given this constraint, the geometric dimensions of the inductive coils and capacitive plates are interrelated, directly affecting electrical parameters. In Fig. 5, the single hybrid magnetic-electric configuration represents one hybrid magnetic-electric coupler, while the dual-channel configuration consists of two such couplers achieving the same-sided magnetic-electric decoupling. As shown in Fig. 5(a), reducing the overlapping area of the capacitive plates leads to a decrease in both self-capacitance and mutual capacitance. In the dual-channel system, the mutual capacitance between adjacent channels is nearly zero due to the symmetrical layout. This spatial separation causes most electric field lines to terminate within each individual channel, resulting in negligible field overlap between different channels. However, the presence of adjacent plates introduces additional electric field interactions. Specifically, these nearby plates induce edge-related surface charges due to fringing fields, effectively forming parasitic paths that do not contribute to cross-channel coupling. These parasitic interactions increase the effective self-capacitance of each plate, as they enhance the distributed capacitance to surrounding conductors or ground. Simultaneously, they intercept a portion of the original coupling field between the transmitter and receiver plates, thereby further reducing the mutual capacitance. This redistribution of electric field lines weakens the intended capacitive coupling. However, when external capacitance is introduced, the degradation in capacitive coupling can be neglected, and both configurations exhibit nearly identical coupling performance.

As shown in Fig. 5(b), both self- and mutual inductance increase with the expansion of the magnetic coupling area due to enhanced magnetic flux. The addition of the dual-channel configuration introduces negligible influence on inductance, suggesting that the spatial decoupling effectively minimizes interchannel magnetic interference and maintains the magnetic integrity of each channel. These results validate the structural feasibility of the dual-channel design. Building upon this foundation, the following section develops a system-level model to quantitatively evaluate the transmission characteristics of the proposed configuration.

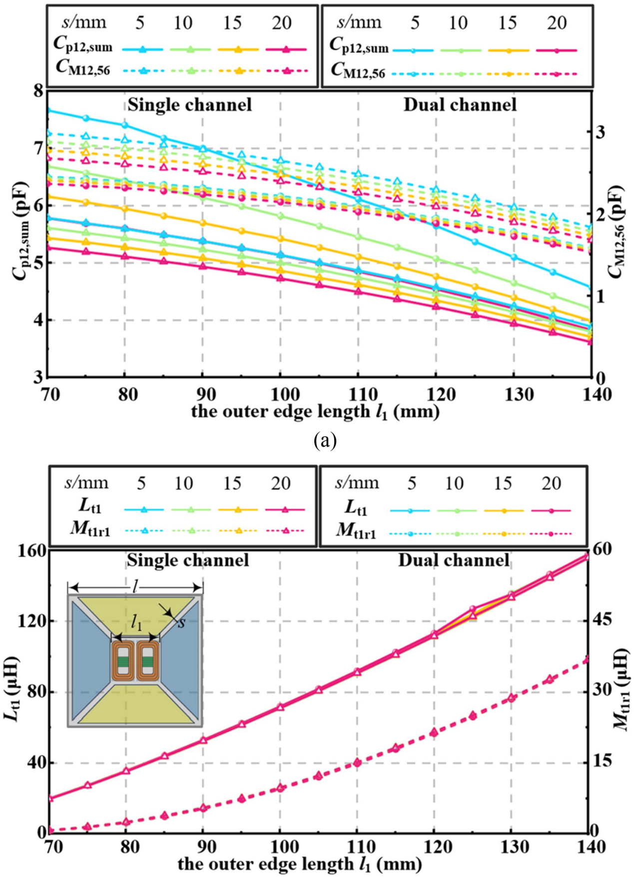

(a)

(b)

Fig. 5. Effect of geometric dimensions on the electrical parameters of the coupler. (a) Capacitance. (b) Inductance.

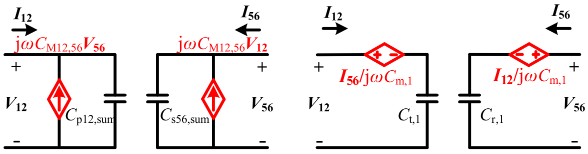

(a) (b)

Fig. 6. Capacitive coupler models. (a) ICS model. (b) IVS model.

III. SYSTEM ANALYSIS

A. Impedance Network Analysis

Typically, coupled inductors are equivalently modeled using an induced voltage source (IVS), while capacitive couplers are represented by a controlled current source (ICS), as shown in Fig. 6(a). For analytical consistency, the capacitive coupler is

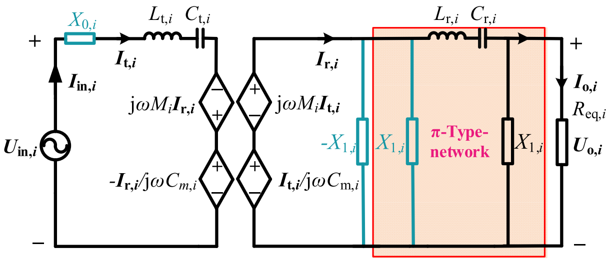

Fig. 7. Equivalent single-channel circuit model of the proposed HWPT system.

converted to an IVS model in Fig. 6(b), enabling a unified modeling framework and simplifying subsequent analysis.

Since the couplers and compensation networks of the two hybrid energy transfer channels are identical, the analysis is performed using the equivalent circuit of a single hybrid energy transfer channel. Take Channel *i* as an example. $C_{\mathrm{t},i}$ and $C_{\mathrm{r},i}$ are the self-capacitances of the transmitter and receiver sides. $C_{\mathrm{m},i}$ is the mutual capacitance. These parameters satisfy (4) shown at the bottom of this page, where $i = 12$ denotes the channel 1 and channel 2, respectively.

Fig. 7 shows the equivalent circuit of a single-channel compensation circuit. In this circuit, $R_{\mathrm{eq},i} = 8R_{\mathrm{L},i}/\pi^2$ is the equivalent resistance at the rectifier terminals. For simplicity, parasitic resistances in the compensation circuit are neglected due to their small values. Reactance $X_{0,i}$ and $X_{1,i}$ serve as compensation components for the system's reactive power. $X_{1,i}$ and $-X_{1,i}$ function as virtual compensation components to achieve constant voltage output. The resonance condition satisfies

$$\begin{cases} X_{1,i} = \frac{1}{\omega C_{\mathrm{r},i}} - \omega L_{\mathrm{r},i} \\ X_{0,i} = \frac{1}{\omega^2 C_{\mathrm{t},i}} - \left(\omega M_{\mathrm{tiri}} + \frac{\alpha}{\omega C_{\mathrm{m},i}}\right)^2 \frac{1}{X_{1,i}} - \omega L_{\mathrm{t},i} \end{cases} \tag{5}$$

where ω represents the operational angular frequency of the system. It can be observed that $X_{1,i}$ is only related to the self-inductance and self-capacitance on the receiving side. Under this resonance condition, $\boldsymbol{I}_{\mathbf{in},i}$ can be derived as

$$\boldsymbol{I}_{\mathbf{in},i} = \frac{X_{1,i}^2}{\left(\omega M_{\mathrm{tiri}} + \alpha \big/ \omega C_{\mathrm{m},i}\right)^2 R_{\mathrm{eq},i}} \boldsymbol{U}_{\mathbf{in},i}. \tag{6}$$

The gain G_i for achieving load-independent constant voltage (CV) output satisfies

$$G_i = \frac{\boldsymbol{U}_{\mathbf{o},i}}{\boldsymbol{U}_{\mathbf{in},i}} = -\frac{X_{1,i}}{\omega M_{\mathrm{tiri}} + \alpha/\omega C_{\mathrm{m},i}}. \tag{7}$$

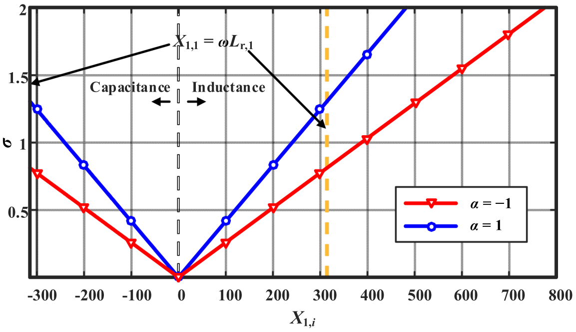

Fig. 8. Variation of σ with $X_{1,i}$ when the component is an inductor or a capacitor.

From (7), it can be seen that the system gain is relevant to the factor α, the mutual inductance $M_{\mathrm{t}i\mathrm{r}i}$, the mutual capacitance $C_{\mathrm{m},i}$, and the reactance $X_{1,i}$. It should be noted that $X_{1,i}$ can be either an inductance or a capacitance, as determined by the compensation condition described in (5). A parameter $\sigma = G_{\mathrm{HWPT}}/G_{\mathrm{IPT}}$ is introduced to quantify the voltage gain enhancement achieved by the HWPT system relative to a conventional IPT system, serving as an indicator of the system's voltage boosting ability.

Fig. 8 illustrates the variation of σ and $X_{1,i}$ for different compensation components under both inductive and capacitive implementations. When $X_{1,i} < 0$, there exists $X_{1,i} > -\omega L_{\mathrm{r},i}$, resulting in σ being limited by the compensation inductance. In contrast, inductive compensation allows broader gain adjustment and is, therefore, adopted in this work. Furthermore, the forward coil connection ($\alpha = 1$) offers a wider gain range compared to the reverse configuration ($\alpha = -1$).

While inductive compensation enhances voltage gain, it also affects system efficiency. In high-gain scenarios, the input resistance R_{in} is inversely proportional to the square of the voltage gain G_i. As a result, high gain leads to significantly low input resistance and increased input current, which in turn amplifies conduction losses—especially those associated with the series inductor. These losses, primarily dissipated as heat, become more pronounced as the gain increases. Thus, minimizing the parasitic resistance of the series inductor is essential for maintaining high efficiency.

To address this issue, a parametric resonance compensation scheme is proposed using external capacitors $C_{\mathrm{ex1},i}$ and $C_{\mathrm{ex2},i}$. According to (5) and (7), once the coupler parameters are fixed, the target gain G_i in the S-SP topology can be determined. Meanwhile, $C_{\mathrm{ex1},i}$ is designed to achieve a zero phase angle.

$$\begin{cases} C_{\mathrm{t},i} = \frac{(C_{\mathrm{p}(2i-1)2i,\mathrm{sum}}+C_{\mathrm{ex1},i})(C_{\mathrm{s}(2i+3)(2i+4),\mathrm{sum}}+C_{\mathrm{ex2},i})-C^2_{\mathrm{M}(2i-1)2i,(2i+3)(2i+4)}}{C_{\mathrm{s}(2i+3)(2i+4),\mathrm{sum}}+C_{\mathrm{ex2},i}} \\ C_{\mathrm{r},i} = \frac{(C_{\mathrm{p}(2i-1)2i,\mathrm{sum}}+C_{\mathrm{ex1},i})(C_{\mathrm{s}(2i+3)(2i+4),\mathrm{sum}}+C_{\mathrm{ex2},i})-C^2_{\mathrm{M}(2i-1)2i,(2i+3)(2i+4)}}{C_{\mathrm{p}(2i-1)2i,\mathrm{sum}}+C_{\mathrm{ex1},i}} \\ C_{\mathrm{m},i} = \frac{(C_{\mathrm{p}(2i-1)2i,\mathrm{sum}}+C_{\mathrm{ex1},i})(C_{\mathrm{s}(2i+3)(2i+4),\mathrm{sum}}+C_{\mathrm{ex2},i})-C^2_{\mathrm{M}(2i-1)2i,(2i+3)(2i+4)}}{C_{\mathrm{M}(2i-1)2i,(2i+3)(2i+4)}} \end{cases} \tag{4}$$

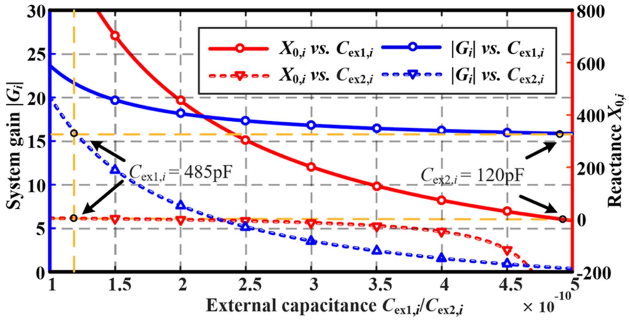

Fig. 9. Effects of external capacitors on system gain and compensation impedance.

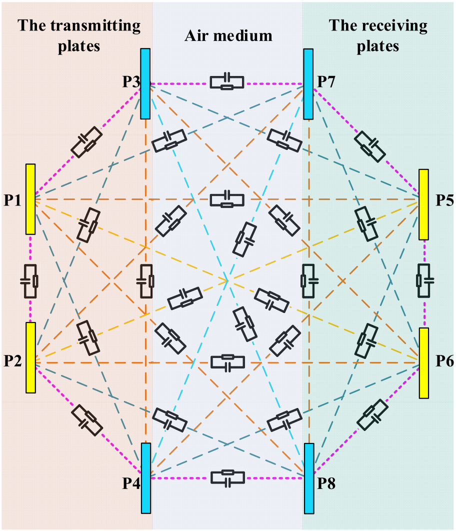

Fig. 10. Capacitive couplings in an eight-plate capacitive coupler considering the parasitic resistances.

Fig. 9 illustrates the relationship between system gain and the impedance $X_{0,i}$ after decoupling the external capacitors $C_{ex1,i}$ and $C_{ex2,i}$. When $C_{ex1,i}$ is varied while holding $C_{ex2,i} = 120$ pF, the impedance $X_{0,i}$ changes significantly, whereas the system gain remains nearly constant. Conversely, when $C_{ex1,i}$ is set to 485 pF, adjusting $C_{ex2,i}$ modulates the system gain without affecting $X_{0,i}$. This behavior clearly demonstrates a functional decoupling: $C_{ex1,i}$ primarily controls the impedance $X_{0,i}$ in the range of 400–500 pF, while $C_{ex2,i}$ governs gain tuning within 100–200 pF. This separation not only enhances system tunability but also facilitates compact integration of the compensation and coupling structures, with broad applicability across various hybrid WPT configurations.

B. Transmission Power Analysis

To investigate the impact of parasitic resistances on system performance, this section constructs a detailed equivalent circuit model consisting of eight capacitive plates. As shown in Fig. 10, in the proposed circuit model, the coupling between any two capacitive plates is represented by a parallel connection of a coupling capacitor and a parasitic resistor, thereby forming a composite admittance network composed of 28 admittance elements. Considering the relatively weak electric field coupling in air at a frequency of 1 MHz, it is assumed that all coupling paths share a uniform quality factor Q. This allows for an indirect assessment of the contribution of parasitic resistance to system losses [27], and the resulting admittance elements are denoted as Y_{mn} (m,n = 12, …,8)

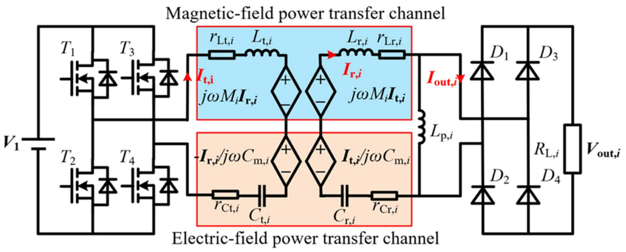

Fig. 11. Equivalent circuit of hybrid system with parasitic resistance.

$$Y_{mn} = \omega C_{mn}\left(j+\frac{1}{Q}\right), (m,n=1,2,\cdots,8). \tag{8}$$

This full admittance model can be converted into a multiport network. The eight plates are grouped into four ports: P1-P2 form port a, P3-P4 form port b, P5-P6 form port c, and P7-P8 form port d. The voltage-current relationships among the eight plates can be described using matrix equations [28], [29]

$$\begin{bmatrix} I_a \\ I_b \\ I_c \\ I_d \end{bmatrix} = \begin{bmatrix} Y_a & -Y_{ab} & -Y_{ac} & -Y_{ad} \\ -Y_{ba} & Y_b & -Y_{bc} & -Y_{bd} \\ -Y_{ca} & -Y_{cb} & Y_c & -Y_{cd} \\ -Y_{da} & -Y_{db} & -Y_{dc} & Y_d \end{bmatrix} \cdot \begin{bmatrix} V_a \\ V_b \\ V_c \\ V_d \end{bmatrix}. \tag{9}$$

The terms Y_a, Y_b, Y_c, and Y_d represent the self-admittances of the four ports, while Y_{ab}, Y_{ba}, Y_{ac}, Y_{ca}, Y_{ad}, Y_{da}, Y_{bc}, Y_{cb}, Y_{bd}, Y_{db}, Y_{cd}, and Y_{dc} represent the mutual admittances between pairs of ports. From (8), (9) can be derived as

$$\mathbf{I}=\mathbf{Y}\cdot\mathbf{V}\Rightarrow\mathbf{I}=\omega\mathbf{C}\cdot\left(\mathrm{j}+\frac{1}{Q}\right)\mathbf{V}=\mathrm{j}\omega\mathbf{C}\cdot\mathbf{V}+\mathbf{R}\cdot\mathbf{V}. \tag{10}$$

I and **V** represent the column vectors of port currents and voltages, respectively; **Y** and **C** denote the four-port admittance and capacitance matrices, while **R** correspond to the four-port resistance matrices. Equation (10) indicates that the equivalent circuit of the proposed coupler can be regarded as the superposition of capacitances and parasitic resistances, which can be calculated independently without requiring all the admittance parameters.

As shown in Fig. 11, $r_{Lt,i}$ and $r_{Lr,i}$ denote the parasitic resistances of the transmitting and receiving coils, respectively. $r_{Ct,i}$ and $r_{Cr,i}$ represent the equivalent parasitic resistances of the capacitive coupler on the transmitting and receiving sides, including the parasitic resistances of external capacitors, plates, and the equivalent resistance from eddy current losses.

The inductive power P_M and capacitive power P_C can be expressed as

$$P_M = \mathrm{Re}\left(j\omega\alpha M_{tiri}\boldsymbol{I}_{r,i}\cdot(-\boldsymbol{I}_{t,i})^*\right) \tag{11}$$

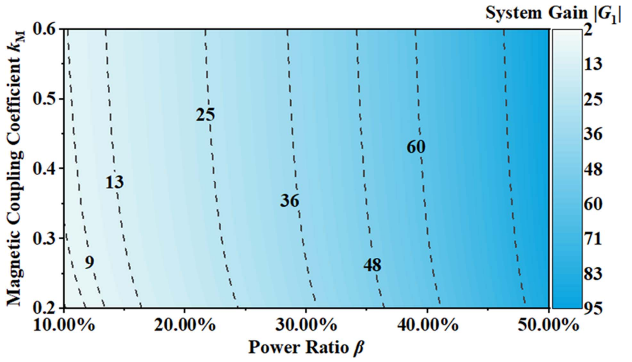

Fig. 12. Impact of magnetic coupling coefficient and power ratio on the system gain.

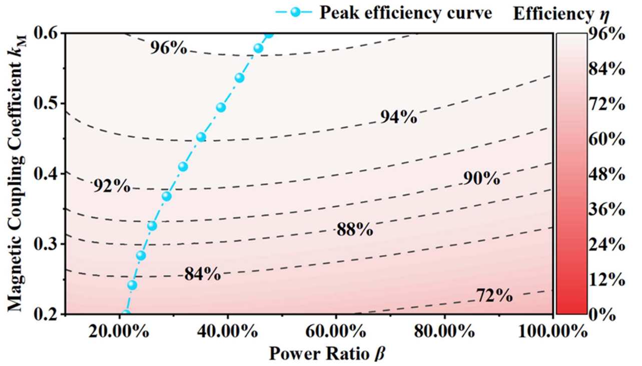

Fig. 13. Impact of magnetic coupling coefficients and power ratio on the system efficiency.

$$P_{\mathrm{C}} = Re\left(-\frac{\boldsymbol{I}_{\mathrm{r},i} \times (-\boldsymbol{I}_{\mathrm{t},i})^*}{j\omega C_{\mathrm{m},i}}\right). \tag{12}$$

Based on (11) and (12), the power ratio β between the electric field power and magnetic field power can be defined as

$$\beta = \frac{P_{\mathrm{C}}}{P_{\mathrm{M}}} = \frac{1}{-\omega^2 C_{\mathrm{m},i}\alpha M_{\mathrm{tiri}}}. \tag{13}$$

From (13), it is evident that β is related to the equivalent parameters of the coupler, ω, and α. In the case of a positive connection, β is negative, and the system's transmission power is the difference between the magnetic field power and the electric field power of the transmission channel. Thus, by changing the area ratio of the magnetic field and electric field coupling mechanisms, β can be adjusted, which in turn adjusts the voltage gain G_i

$$G_i = \frac{\alpha}{k_{\mathrm{E},i}(1+\beta)} + \frac{\beta}{k_{\mathrm{M},i}(1+\beta)} \tag{14}$$

where $k_{\mathrm{E},i} = C_{\mathrm{r},i}/\ C_{\mathrm{m},i}$, $k_{\mathrm{M},i} = M\ /\ L_{\mathrm{r},i}$. Fig. 12 presents the system gain analysis concerning the magnetic coupling coefficient $k_{\mathrm{M},i}$ and the power ratio β. As β increases, the gain rises progressively with an accelerating growth rate. For $\beta <$ 20%, the gain exhibits slight improvement with increasing $k_{\mathrm{M},i}$, indicating limited sensitivity in low-gain regions. However, for $\beta >$ 20%, corresponding to high-gain scenarios, the influence of $k_{\mathrm{M},i}$ on gain becomes negligible. It should be noted that (14) decomposes the contributions of magnetic and electric field coupling to the overall gain. Magnetic coupling enables energy transfer via mutual inductance between coils, while electric coupling operates through capacitive interaction between plates. At low power ratios, the contribution from electric coupling is minimal, and magnetic coupling dominates the gain. As the power ratio increases, electric field coupling becomes more significant and gradually emerges as the primary contributor to gain enhancement.

Since the coupler is symmetric, $r_{\mathrm{Lt},i} = r_{\mathrm{Lr},i}$, and $r_{\mathrm{Ct},i} = r_{\mathrm{Cr},i}$. The transmission efficiency η_{all} can be further expressed as

$$\eta_{\mathrm{all}} = \frac{\boldsymbol{I}_{\mathrm{out},i}^2 R_{\mathrm{eq},i}}{1 + \boldsymbol{I}_{\mathrm{in},i}^2 (r_{\mathrm{Lt},i} + r_{\mathrm{Ct},i}) + \boldsymbol{I}_{\mathrm{r},i}^2 (r_{\mathrm{Lr},i} + r_{\mathrm{Cr},i})}$$

$$= \frac{1}{1 + G_i^2 \frac{Q_{\mathrm{L},i} + k_{\mathrm{M},i}^2 (1+\beta)^2 Q_{\mathrm{L},i}^3}{(Q_{\mathrm{Lr},i} - Q_{\mathrm{L},i})\beta^2} + G_i^2 \frac{Q_{\mathrm{C},i} + k_{\mathrm{E},i}^2 (1+\beta)^2 Q_{\mathrm{C},i}^3}{Q_{\mathrm{Cr},i} - Q_{\mathrm{C},i}}} \tag{15}$$

where $Q_{\mathrm{Lr},i}$ represents the quality factor of the receiver coil, $Q_{\mathrm{L},i}$ represents the quality factor of the receiving end, $Q_{\mathrm{Cr},i}$ represents the quality factor of the receiver capacitor, and $Q_{\mathrm{C},i}$ denotes the quality factor of the receiving end and are defined as

$$\begin{aligned} Q_{Lr,i} &= \frac{\omega L_{\mathrm{r},i}}{r_{Lr,i}} Q_{L,i} = \frac{\omega L_{\mathrm{r},i}}{r_{Lr,i} + R_{\mathrm{eq},i}} \\ Q_{Cr,i} &= \frac{1}{\omega C_{\mathrm{r},i} r_{\mathrm{Cr},i}} Q_{C,i} = \frac{1}{\omega C_{\mathrm{r},i}(r_{\mathrm{Cr},i} + R_{\mathrm{eq},i})}. \end{aligned} \tag{16}$$

To ensure that the transmission efficiency of the proposed HWPT system is higher than that of the conventional IPT system, the following inequality (17) must be satisfied:

$$\begin{aligned} &G_i^2 \frac{Q_{L,i} + k_{M,i}^2 (1+\beta)^2 Q_{L,i}^3}{(Q_{Lr,i} - Q_{L,i})\beta^2} + G_i^2 \frac{Q_{C,i} + k_{E,i}^2 (1+\beta)^2 Q_{C,i}^3}{Q_{Cr,i} - Q_{C,i}} \\ &< G_{\mathbf{IPT}}^2 \frac{{Q_L}^2 \left(1 + 1/\, k_{\mathbf{IPT}}^2\right)}{Q_{\mathbf{Lr}}(Q_{\mathbf{Lr}} - Q_L)^2}. \end{aligned} \tag{17}$$

As shown in Fig. 13, the system efficiency initially increases and then decreases with the increasing power ratio β, exhibiting only slight variation overall. A peak efficiency point is observed, beyond which, when $\beta >$ 50%, efficiency drops. This decline is attributed to the opposing power transmission directions between the magnetic and electric field coupling channels, resulting in reduced net power transfer. System efficiency also improves with increasing magnetic coupling coefficient, showing a more pronounced variation, consistent with general trends in WPT system design. When both the magnetic coupling coefficient and power ratio vary simultaneously, an optimal region for maximizing efficiency is identified within the range $\beta \in$(20%, 50%). In this range, higher magnetic coupling and optimal power ratios collectively enhance system performance.

C. Comparison of HWPT With IPT System

To evaluate the transmission efficiency of the proposed HWPT system, a conventional IPT system as a benchmark. In the IPT

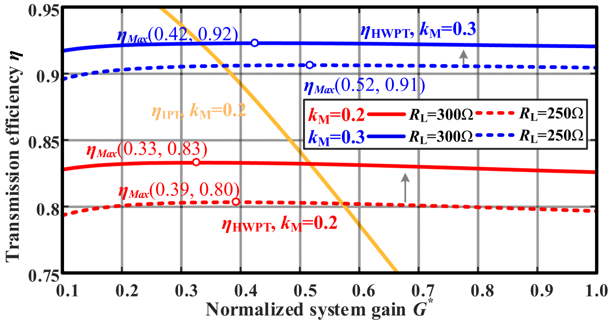

Fig. 14. Comparison of the proposed HWPT system to the IPT system.

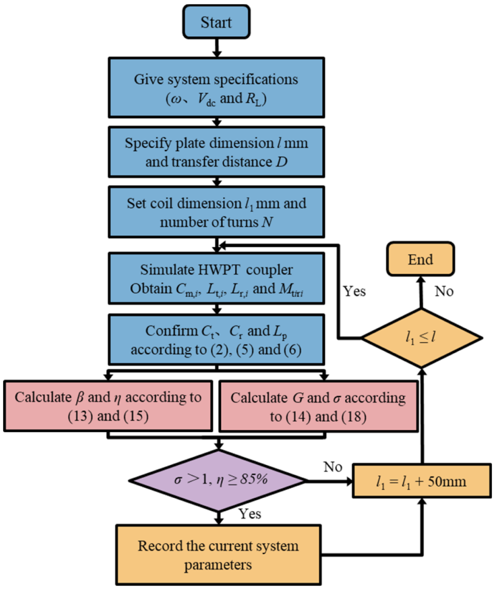

Fig. 15. Design process of the proposed system.

system, the receiving end adopts an SP compensation topology, consisting of a series capacitor C_r and a parallel inductor L_p. The corresponding voltage gain is expressed by

$$G_{\mathbf{IPT}} = \frac{L_\mathrm{p}}{M} = \frac{1}{k_{\mathrm{IPT}}} - \frac{1}{\omega^2 M C_\mathrm{r}}. \tag{18}$$

It can be seen that the gain is inversely proportional to the coupling coefficient, so it is challenging for the system to achieve both high voltage gain and efficient power transfer. The IPT system efficiency can be obtained, as shown in

$$\eta_{\mathbf{IPT}} = \frac{1}{1 + G_{\mathrm{IPT}}^2 \frac{{Q_L}^2\left(1+1/k_{\mathrm{IPT}}^2\right)}{Q_{\mathrm{Lr}}\left(Q_{\mathrm{Lr}}-Q_L\right)^2}}. \tag{19}$$

Similarly, the output gain of the HWPT system can be derived as

$$G_{\mathbf{HWPT}} = -\frac{L_{\mathrm{p},i}}{M_{\mathrm{t}i\mathrm{r}i}}\left(1 - \frac{1}{1+\beta}\right). \tag{20}$$

Fig. 14 illustrates the variation in transmission efficiency with normalized voltage gain for both IPT and HWPT systems employing SP compensation. As shown in Fig. 15, transmission efficiency initially increases with gain but declines beyond a certain threshold. Despite this decline, the HWPT system sustains significantly higher efficiency under high-gain conditions compared to the IPT counterpart. Furthermore, efficiency improves with increasing load resistance, reinforcing the dependence of high-gain performance on input impedance. Notably, the proposed system maintains efficiency above 85% while achieving high voltage gain, demonstrating its ability to deliver both high gain and high energy transfer efficiency simultaneously. The proposed dual-channel HWPT system, based on magneto-electric hybrid coupling, exhibits notable performance advantages.

In summary, the proposed HWPT system introduces a CPT subsystem with reverse power transfer to adjust the power ratio β between electric and magnetic transmission channels, thereby expanding the voltage gain tuning range. This innovative design addresses the inherent tradeoff between efficiency and voltage gain observed in standalone IPT systems, achieving high-gain output while maintain high efficiency. Notably, the voltage gain enhancement is equivalent to cascading a gain factor 1-1/(1+β) on the output side, amplifying system performance through multiplicative interaction rather than linear superposition.

D. Parameter Design and Simulation

In this section, the HWPT system design method is discussed. According to (10), a low operating frequency leads to a significant decrease in the proportion of power transmitted through electric-field and the magnetic-field coupling channels, which in turn complicates the design of the compensation network parameters and hindering efficiency optimization. On the other hand, a high operating frequency increases of the contribution of capacitive power transfer. However, it also exacerbates skin effect in conductors, particularly in the compensation network and interconnecting elements, which increases parasitic resistance and conduction losses. This effect becomes especially pronounced in the capacitive plates and consequently reducing system efficiency. Considering these tradeoffs and prior HWPT research, the operating frequency of the proposed system is set at 1 MHz to balance efficiency and design complexity.

The optimization process of the hybrid coupler is shown in Fig. 15. To achieve a HWPT system with both high voltage gain and high efficiency, this section introduces two optimization parameters, η and σ, as indicators for evaluating system efficiency and gain. These optimization parameters are applied to the design of the integrated magnetic-electric coupler. First, the system's operating frequency, input voltage, and load resistance are determined based on the specific application scenario. The coupling mechanism's size l and transmission distance D are defined accordingly. By establishing a finite element simulation model of the hybrid coupler, C_M, M, L_t, and L_r under different area ratios are obtained. Based on (2), (5), and (6), the compensation network parameters and external capacitors C_{ex1} and C_{ex2} are determined. Subsequently, the system efficiency and voltage enhancement capability σ are calculated using (14) and (18). Power ratio and efficiency are then computed based on (13) and (15). Finally, the Coil's length l_1 is adjusted iteratively, recording

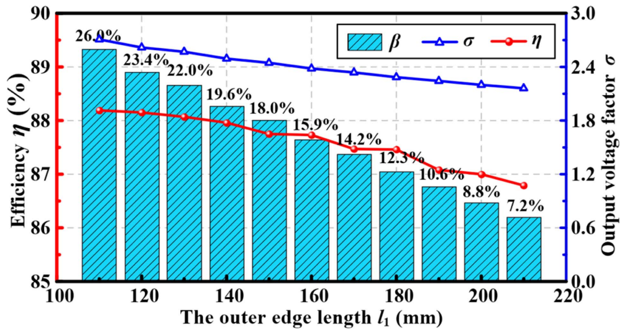

Fig. 16. Power ratio, efficiency, and output voltage factor σ versus plate size.

the optimal system parameters that satisfy the conditions $\eta \geq 85\%$ and $\sigma > 1$.

Fig. 16 illustrates the impact of increasing the coil edge length l_1 from 100 mm to 220 mm on the power ratio coefficient β, system efficiency, and coupling coefficient σ. The power ratio coefficient β decreases monotonically from 26% to 7.2%, indicating a gradual reduction in the power transfer capability of the capacitive coupling channel. This decline is primarily attributed to the substantial decrease in equivalent coupling capacitance as the plate area is reduced. Notably, at a coil size of 120 mm, the power transfer performance improves by 1.4 compared to the baseline G_{IPT}.

E. Voltage Stress Analysis of the Capacitive Plates

To evaluate the voltage stress on the capacitive plates of the proposed HWPT system, a comprehensive analysis was conducted through theoretical modeling, circuit-level simulation, and finite element analysis. Under the resonance condition adopted in this work, the currents $I_{\mathrm{t},1}$ and $I_{\mathrm{r},1}$ can be expressed as

$$\begin{cases} I_{\mathrm{t},i} = \frac{U_{\mathrm{in}} \cdot G_i^2}{R_{\mathrm{eq},i}} \\ I_{\mathrm{r},i} = \frac{U_{\mathrm{in}} \cdot G_i}{R_{\mathrm{eq},i} \| j\omega L_{\mathrm{p},i}}. \end{cases} \tag{21}$$

The same-side inter-plate (SIP) voltages U_{SIP} across the capacitive plates are obtained as

$$\begin{aligned} \boldsymbol{V}_{(2i-1)2i} &= \boldsymbol{U}_{\mathrm{in}} - j\omega L_{\mathrm{t},i} \boldsymbol{I}_{\mathrm{t},i} + j\omega M_{\mathrm{tiri}} \boldsymbol{I}_{\mathrm{r},i} \\ \boldsymbol{V}_{(2i+3)(2i+4)} &= j\omega M_{\mathrm{tiri}} \boldsymbol{I}_{\mathrm{t},i} + j\omega L_{\mathrm{r},i} \boldsymbol{I}_{\mathrm{r},i} + \boldsymbol{U}_{\mathrm{in}} G_i. \end{aligned} \tag{22}$$

By substituting (21) into (22), $V_{(2\mathrm{i}-1)2\mathrm{i}}$ and $V_{(2\mathrm{i}+3)(2\mathrm{i}+4)}$ can be rewritten as

$$\begin{aligned} \boldsymbol{V}_{(2i-1)2i} &= \boldsymbol{U}_{\mathrm{in}} \left(1 + \frac{\omega M_{\mathrm{tiri}}}{A}\right) \\ &\quad + j \cdot \boldsymbol{U}_{\mathrm{in}} \left(\frac{\omega M_{\mathrm{tiri}} G_i}{R_{\mathrm{eq},i}} - \frac{\omega L_{\mathrm{t},i} G_i^2}{R_{\mathrm{eq},i}}\right) \\ \boldsymbol{V}_{(2i+3)(2i+4)} &= \boldsymbol{U}_{\mathrm{in}} \left(G_i + \frac{\omega L_{\mathrm{r},i}}{A}\right) \\ &\quad + j \cdot \boldsymbol{U}_{\mathrm{in}} \left(\frac{\omega M_{\mathrm{tiri}} G_i^2}{R_{\mathrm{eq},i}} + \frac{\omega L_{\mathrm{r},i} G_i}{R_{\mathrm{eq},i}}\right) \end{aligned} \tag{23}$$

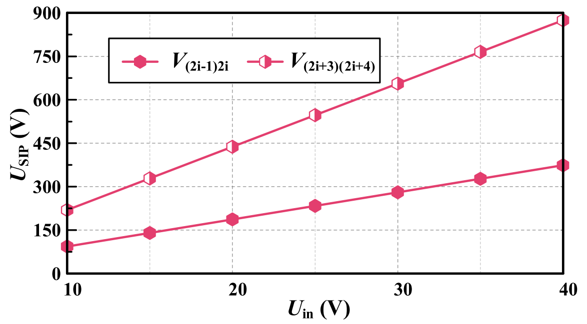

Fig. 17. SIP voltage with different input voltages.

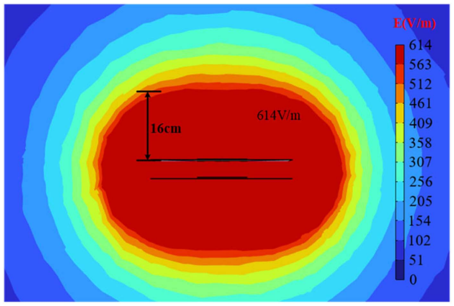

Fig. 18. Electric field distribution of the coupler.

where A is defined as

$$A = \omega M_{\mathrm{tiri}} - \frac{1}{\omega C_{\mathrm{m},i}}. \tag{24}$$

Equation (23) reveals the quantitative relationship between the port voltage in the capacitive path and key system parameters. Specifically, the plate voltage exhibits a linear dependence on the input voltage. The SIP voltages of the capacitive plates under different input voltages are shown in Fig. 17. The results indicate that the SIP voltage remains below 1 kV when the input voltage varies between 10 V and 40 V, thereby ensuring safe operation within the defined insulation limits.

To further evaluate the safety margin from the perspective of spatial field distribution, a finite element static electric field model was developed for full-domain analysis of the capacitive plates. As illustrated in Fig. 18, the electric field is uniformly distributed in the central region of the plates, while localized field concentration occurs near the edges. According to IEEE standards, the human exposure safety limit for electric fields at 1 MHz is 614 V/m. In the maximum excitation scenario, the contour associated with this standard lies approximately 16 cm away from the outer edge of the plate, further confirming the compliance of the proposed system with exposure safety requirements. In the proposed HWPT topology, electric-field-based power transfer contributes only about 20% of the total transferred power, with the majority handled by magnetic field coupling. Consequently, the voltage stress imposed on the capacitive plates remains relatively low. At standard temperature and pressure, the breakdown electric field strength of air is approximately 3 kV/mm. Considering additional risk factors such as edge field concentration, surface contamination, and

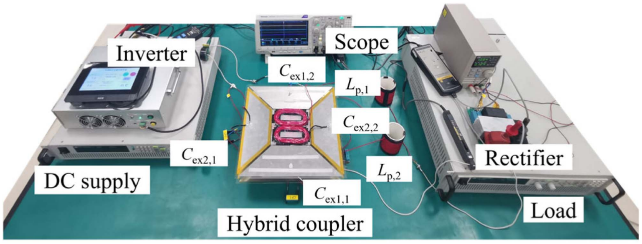

Fig. 19. Experimental prototype of the HWPT system.

TABLE II
SYSTEM PROTOTYPE CIRCUIT PARAMETERS

Parameter	Value	Parameter	Value
U_{DC}	30 V	f	1000 kHz
L_{t1}	39 μH	$C_{12,sum}$	408.9 pF
L_{t2}	39.9 μH	$C_{34,sum}$	410.2 pF
L_{r1}	36.7 μH	$C_{56,sum}$	227.7 pF
L_{r2}	36 μH	$C_{78,sum}$	228.2 pF
M_{t1t2}/	0.15 μH	$C_{M12,34}$	0.62 fF
M_{t1r1}/μH	7.65 μH	$C_{M12,56}$	4.24 pF
M_{t1r2}/μH	0.55 μH	$C_{M12,78}$	0.23 fF
M_{t2r1}/μH	0.42 μH	$C_{M34,56}$	0.11 fF
M_{t2r2}/μH	7.1 μH	$C_{M34,78}$	4.86 pF
M_{r1r2}/μH	0.59 μH	$C_{M56,78}$	0.55 fF
$L_{p,1}/\mu$H	39.6 μH	$L_{p,2}/\ \mu$H	40.5 μH
$r_{Lt,1}$	0.69 Ω	$r_{Ct,1}$	0.19 Ω
$r_{Lt,2}$	0.59 Ω	$r_{Ct,2}$	0.13 Ω
$r_{Lr,1}$	0.88 Ω	$r_{Cr,1}$	0.15 Ω
$r_{Lr,2}$	0.57 Ω	$r_{Cr,2}$	0.16 Ω

electrode oxidation, a safety margin of three to five times the theoretical breakdown strength was applied to ensure insulation reliability under practical operating conditions. In this design, the minimum spacing between adjacent capacitive plates is set to 5 mm, which prevents breakdown under high-frequency and high-voltage excitation.

IV. EXPERIMENT

A. Experimental Setup

An experimental prototype was constructed to validate the proposed HWPT system, as shown in Fig. 19. The system specifications and circuit parameters are listed in Table II. The coupling coils and compensation inductors use 0.04 × 2000 strand twisted Litz wire to mitigate the skin effect. The compensation inductors are wound on PVC hollow tubes to reduce the resistive losses of the inductance. The capacitive coupler is made of 2 mm thick aluminum plates, where the dimensions of the transmitter plates P_1, P_2, P_3, and P_4 are the same as those of the receiver plates P_5, P_6, P_7, and P_8. The external capacitors are formed into a high-voltage capacitor module by series and parallel connection of KEMET high-frequency film capacitors, with a maximum peak ac rated voltage of 700 V and a capacitance tolerance of ±5%. Furthermore, to prevent breakdown and leakage, the entire hybrid magnetic-electric coupler is mounted on a 5 mm thick transparent epoxy resin board. A wide-bandgap SiC MOSFET (C3M0075120D) is used in the inverter to provide high-frequency ac excitation. The SiC MOSFETs were driven using UCC21520 isolated gate drivers with a gate voltage of +15 V/-4 V and an external gate resistor of 5 Ω to ensure proper switching performance and noise immunity. A digital controller (TMS320F28335) generates pulsewidth modulation signals to drive the SiC MOSFETs at a switching frequency of 1 MHz.

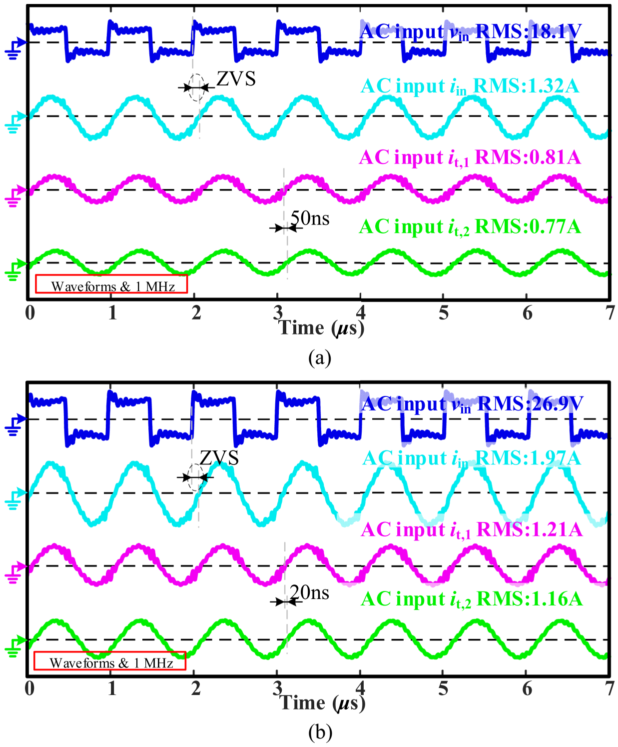

(a)

(b)

Fig. 20. Experimental input waveforms of a two-channel system at different input. (a) 20 V. (b) 30 V.

B. Experimental Results

In practical experiments, although theoretical models predict zero mutual inductance between orthogonally arranged DD coils aligned along the x- and y-axes, residual cross-coupling is often observed. This deviation arises from the fact that the adjacent coil windings in the two channels are not strictly sym metrical during fabrication, and manual experimental errors distort the magnetic field distribution, resulting in residual coupling. Precise adjustment of the number of turns on each side is, therefore, required to approach the condition of zero mutual inductance. Similarly, although orthogonally arranged plates are theoretically expected to exhibit negligible cross-coupling capacitance, physical misalignments, and nonuniform surface conditions can also lead to residual capacitive coupling under experimental conditions, which is difficult to measure accurately. As a result, the geometric parameters of both the coils and plates are carefully tuned to ensure phase alignment of the input currents in the two transmission channels.

In the dual-channel parallel–series architecture, current balancing on the primary-side parallel structure is constrained by the consistency of the coupling structures' parameters. As shown in Fig. 20, the input current amplitudes for Channel 1 and Channel 2 are $I_{t,1} = 1.21$ A and $I_{t,2} = 1.16$ A, respectively, with a phase error of less than 5°. These electrical parameter

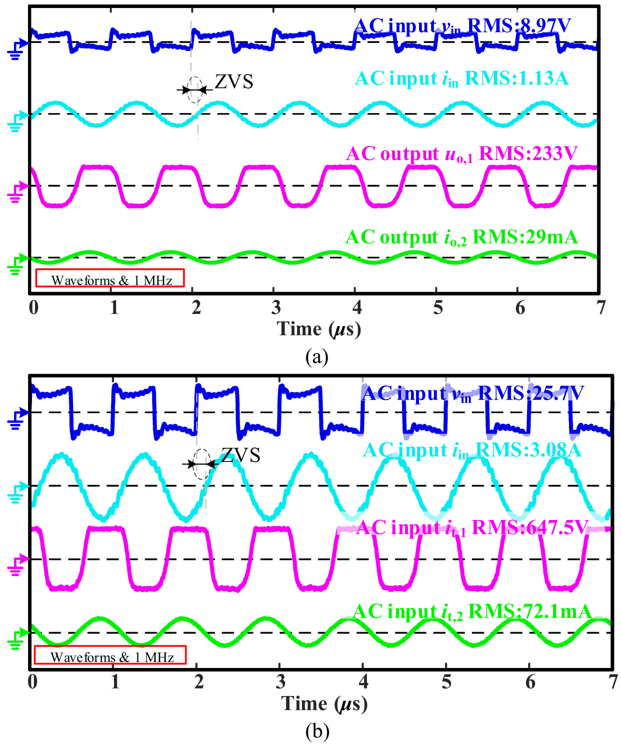

(a)

(b)

Fig. 21. Experimental input and output waveforms of a two-channel system at different input. (a) 20 V. (b) 30 V.

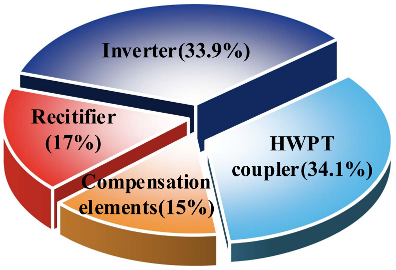

Fig. 22. Power loss distribution of HWPT.

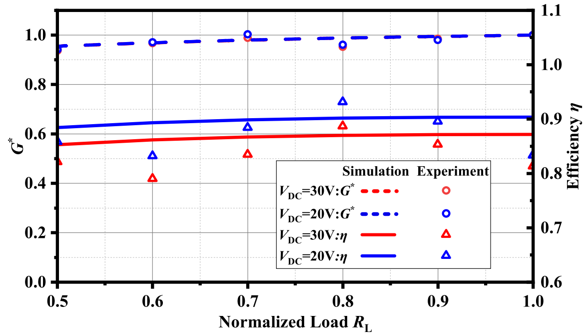

Fig. 23. Measured load voltage and efficiency under different loads.

mismatches primarily lead to differences in the real part of the impedance between channels, resulting in uneven current distribution. However, by tuning the resonant components, the imaginary parts remain synchronized in phase. Additionally, although the orthogonal layout of coils and plates suppresses interchannel coupling, residual cross-coupling inductance can still introduce circulating disturbances into the primary-side parallel loop. This disturbance further affects the inverter's output characteristics. Specifically, due to impedance mismatch, a slight distortion appears in Channel 1's current, manifested as periodic ripple fluctuations near the resonance peak of the inverter output current.

The input and output waveforms of the two-channel system are shown in Fig. 21, and the efficiency reaches 86.5% with an output power of 50 W. During the test period, the full-bridge inverter achieved zero-voltage switching with a shutdown current of about 2.7 A. At 30 V input the two-channel system produces a 25.2 voltage gain at 50 W, with 86.5% dc–dc efficiency output. The results show that the proposed HWPT system can effectively meet the design requirements of high voltage gain.

Based on experimental measurements, Fig. 22 shows the distribution of losses among the circuit components for the system at 50 W output. The total power loss of the system is 10.15 W, which mainly comes from switching devices' switching transitions, the conduction loss and the losses in the integrated coupler. Specifically, after analyzing the system in Section III, the losses in the integrated coupler are small and the inverter and rectifier remain the main source of losses. The body diode plays an important role in the ZVS operation. It has a large reverse recovery charge, which creates difficulties in realizing ZVS and significantly increases the losses in the system at an operating frequency of 1 MHz.

As shown in Fig. 23, the proposed two-channel HWPT system demonstrates load-independent CV output behavior, with the normalized load voltage gain remaining nearly constant across the 0.5–1.0 load range. In terms of efficiency, the system achieves over 85% dc–dc conversion efficiency within the 0.7–0.9 normalized load range under a 30 V dc input, reaching a peak efficiency of 86.5%. The actual measured values are generally consistent with the simulation in the 0.7–0.9 normalized load, while more pronounced deviations occur in other regions, mainly due to differences in the practical quality factor q and additional hardware nonidealities.

C. Performance Comparison

The performance of the proposed dual-channel HWPT system is compared with previous works, as summarized in Table III. To overcome limitations imposed by coil parameters, high-order compensation networks such as *LCL-LCL* and *LCC-LCC* have been employed to constrain voltage gain within a finite range, thereby restoring tunability of the gain [7], [15]. Building upon high-order compensation, Li et al. [15] further introduced frequency modulation to extend the gain range via variable-frequency control. In contrast, the S-CLC-based circuit proposed in [16] achieves wide-range gain tuning solely through capacitive adjustments, without requiring an independent inductor or complex controls. This approach significantly simplifies system integration and reduces design complexity. Xu et al. [24] demonstrated that HWPT systems leveraging both inductive and capacitive transfer paths can surpass standalone IPT and CPT in achievable voltage gain range and efficiency. If the power

TABLE III
COMPREHENSIVE COMPARISON WITH PREVIOUS WORKS

Reference	System	Frequency	Compensation network	Compensating element	CC/CV mode	Gain regulation	Inductor integration	Efficiency in $G_{\max}$
[7]	CPT	1 MHz	*LCL-LCL*	6	CC	Regulate reactance	No	90%
[15]	IPT	85 ±5 kHz	*LCC-LCC*	6	CC	Variable frequency	No	85.3%
[16]	IPT	300 kHz	*S-CLC*	4	CC	Regulate capacitors	Yes	88.9%
[24]	HWPT	6.78 MHz	*S-S*	2	No	Regulate f and Q	Yes	80.02%
[30]	CPT	1 MHz	*LC-LC*	6	CV	Increase channels	No	81.34%
This work	HWPT	1 MHz	*S-SP*	2	CV	Regulate capacitors	Yes	86.5%

transfer ratio between the hybrid branches and the connection mode of receiving coils are further investigated in this system, it is expected to enhance the flexibility of gain regulation. However, this aspect was not discussed in [24]. Furthermore, Zhou et al. [30] proposed a modular multichannel CPT system that employs a scalable electric-field coupler with an ISOS architecture. It leverages shared decoupling inductors to suppress cross-coupling and achieve gain doubling by parallelizing identical ISOS modules.

Therefore, building upon previous studies, this work proposes a dual-channel hybrid wireless power transfer system that effectively broadens the output gain range, which breaks the conventional limitation where the system gain is constrained by magnetic components such as coils or inductors. A dual-channel hybrid coupler with decoupling is integrated into the proposed system to simultaneously support inductive and capacitive power transfer. By employing an asymmetric S-SP compensation network, it enables flexible power allocation between the two channels and achieves wide range gain tuning with constant-voltage output, all without resorting to control strategies or high-order networks.

However, the present work focuses primarily on the modeling and experimental validation of the dual-channel hybrid system. Future research will further optimize and design an integrated magneto-electric coupler to address the performance requirements under lateral and angular misalignments, thereby enhancing the adaptability of the system to diversified application scenarios.

V. CONCLUSION

This article proposes a novel two-channel HWPT system that simultaneously achieves high voltage gain and efficient energy delivery. The system incorporates magnetically coupled and capacitively coupled transmission paths, which operate in a coordinated manner to optimize power transfer. Instead of relying on conventional single-mode or multitransmitter topologies, the proposed design leverages dual-channel hybrid coupling to dynamically tune the power distribution between the two channels, thereby achieving high voltage gain without sacrificing efficiency. Experimental results show that the proposed HWPT system achieves the load-independent CV output with a maximum efficiency of 86.5% and the system gain is 25.2.

REFERENCES

[1] M. Li, X. Zhang, Z. Chen, Z. Dai, and L. Zhao, "A regional coupling enhanced omnidirectional wireless power transfer system with low-fluctuation regulation strategy," *IEEE Trans. Power Electron.*, vol. 40, no. 9, pp. 11918–11922, Sep. 2025.

[2] B. Luo, M. Wang, J. Tang, T. Wang, L. Bai, and J. You, "An underwater simultaneous wireless power and analog-digital hybrid signal transfer system," *IEEE Trans. Power Electron.*, vol. 40, no. 12, pp. 17569–17574, Dec. 2025.

[3] Y. Wu et al., "An integrated charger of wireless power transfer, onboard charger, and auxiliary power module for electric vehicles," *IEEE Trans. Power Electron.*, vol. 40, no. 4, pp. 6334–6344, Apr. 2025.

[4] B. Zhang, C. Q. Jiang, F. Yang, C. Chen, Y. Lu, and J. Zhou, "An antirotation wireless power transfer system with a flexible magnetic coupler for autonomous underwater vehicles," *IEEE Trans. Power Electron.*, vol. 40, no. 1, pp. 2593–2603, Jan. 2025.

[5] M. Liao et al., "UAV fleet charging on telecom towers with differential capacitive wireless power transfer," *IEEE Trans. Power Electron.*, vol. 40, no. 4, pp. 6370–6384, Apr. 2025.

[6] T. Chen, C. Cheng, H. Cheng, C. Wang, and C. C. Mi, "A multi-load capacitive power relay system with load-independent constant current outputs," *IEEE Trans. Power Electron.*, vol. 37, no. 5, pp. 6144–6155, May 2022.

[7] T. Chen, C. Cheng, X. Zhang, G. Li, Y. Guo, and C. C. Mi, "A double-sided LCL-compensated network for the strongly coupled CPT system with minimum plate voltage stresses," *IEEE J. Emerg. Sel. Topics Power Electron.*, vol. 12, no. 4, pp. 4275–4287, Aug. 2024.

[8] Y. Chen et al., "A parameter tuning method for a double-sided compensated IPT system with constant-voltage output and efficiency optimization," *IEEE Trans. Power Electron.*, vol. 38, no. 3, pp. 4124–4139, Mar. 2023.

[9] Y. Wang, J. Yang, K. Wang, and Y. Yang, "Highly integrated hybrid inductive and capacitive power transfer system with asymmetrical printed-circuit-board-based self-resonator," *IEEE Trans. Power Electron.*, vol. 40, no. 7, pp. 10254–10264, Jul. 2025.

[10] F. Wang, Q. Yang, X. Zhang, T. Chen, and G. Li, "Enhancing misalignment tolerance in hybrid wireless power transfer system with integrated coupler via frequency tuning," *IEEE Trans. Power Electron.*, vol. 39, no. 9, pp. 11885–11899, Sep. 2024.

[11] X. Qing, Z. Li, X. Wu, Z. Liu, L. Zhao, and Y. Su, "A hybrid wireless power transfer system with constant and enhanced current output against load variation and coupling misalignment," *IEEE Trans. Power Electron.*, vol. 38, no. 10, pp. 13219–13230, Oct. 2023.

[12] K. Li, J. Wu, S.-C. Tan, K. W. E. Cheng, and S.-Y. R. Hui, "Characterization and modeling of dual-single-layer PCB resonators for mega-hertz hybrid inductive and capacitive wireless power transfer," *IEEE Trans. Power Electron.*, vol. 40, no. 10, pp. 16004–16021, Oct. 2025.

[13] S. Li, K. Xia, T. Li, S. Lu, J. Xia, and Z. Liu, "A novel comb-shaped coupler for hybrid inductive and capacitive wireless power transfer system," *IEEE Trans. Power Electron.*, vol. 40, no. 4, pp. 4787–4792, Apr. 2025.

[14] Y. Xu, Y. Li, Y. Chen, W. Zhou, R. Mai, and Z. He, “A multiple-gain-reconfigurable-rectifier-based IPT system for battery multistage constant-current high-efficiency wireless charging,” *IEEE Trans. Power Electron.*, vol. 39, no. 1, pp. 1853–1869, Jan. 2024.

[15] X. Li, D. Zhou, S. Jia, X. Liu, and J. Zou, “A WPT system with wide-range voltage gains and soft switching via primary-side hybrid modulation,” *IEEE Trans. Power Electron.*, vol. 39, no. 7, pp. 8985–8997, Jul. 2024.

[16] C. Cai, J. Wang, M. Saeedifard, P. Zhang, R. Chen, and J. Zhang, “Gyrator-gain variable WPT topology for MC-unconstrained CC output customization using simplified capacitance tuning,” *IEEE Trans. Ind. Electron.*, vol. 71, no. 4, pp. 3594–3605, Apr. 2024.

[17] W. Liu, J. Lu, C. C. Mi, and K. T. Chau, “Integrated sensorless wireless charging using symmetric high-order network for multistorey car parks,” *IEEE Trans. Power Electron.*, vol. 39, no. 8, pp. 10568–10581, Aug. 2024.

[18] B. Cheng and L. He, “High-order network based general modeling method for improved transfer performance of the WPT system,” *IEEE Trans. Power Electron.*, vol. 36, no. 11, pp. 12375–12388, Nov. 2021.

[19] A. Bagheri and H. Iman-Eini, “A high-voltage capacitor charger based on a novel LCCL resonant converter,” *IEEE Trans. Ind. Electron.*, vol. 69, no. 11, pp. 11046–11054, Nov. 2022.

[20] L. Huang, A. P. Hu, A. K. Swain, and Y. Su, “Z-impedance compensation for wireless power transfer based on electric field,” *IEEE Trans. Power Electron.*, vol. 31, no. 11, pp. 7556–7563, Nov. 2016.

[21] S. Lu, D. Kong, S. Xu, L. Luo, and S. Li, “A high-efficiency 80-kW split planar transformer for medium-voltage modular power conversion,” *IEEE Trans. Power Electron.*, vol. 37, no. 8, pp. 8762–8766, Aug. 2022.

[22] S. Li, X. Yu, Y. Yuan, S. Lu, and T. Li, “A novel high-voltage power supply with MHz WPT techniques: Achieving high-efficiency, high-isolation, and high-power-density,” *IEEE Trans. Power Electron.*, vol. 38, no. 12, pp. 14794–14805, Dec. 2023.

[23] Y. Liang et al., “Analysis and parameter design for input-series output-series (ISOS) multichannel inductive power transfer system considering cross coupling,” *IEEE J. Emerg. Sel. Topics Power Electron.*, vol. 12, no. 2, pp. 2361–2376, Apr. 2024.

[24] C. Xu, Y. Shengbao, S. Shuchao, T. H. Li River, Y. Xiaobo, and Z. Zhe, “Hybrid coupler for 6.78 MHz desktop wireless power transfer applications with stable open-loop gain,” *Int. Eng. Technol. Power Electron.*, vol. 12, no. 10, pp. 2642–2649, 2019.

[25] X. Zhang, G. Li, T. Chen, F. Wang, Q. Yang, and W. Xu, “A high-efficiency underwater hybrid wireless power transfer system with low plate voltage stresses,” *IEEE Trans. Power Electron.*, vol. 39, no. 8, pp. 10546–10557, Aug. 2024.

[26] F. Wang, Q. Yang, X. Zhang, T. Chen, A. P. Hu, and G. Li, “Near field electromagnetic energy flow regulation method for WPT system via frequency adjustment,” *IEEE J. Emerg. Sel. Topics Power Electron.*, vol. 13, no. 4, pp. 4060–4073, Aug. 2025.

[27] H. Zhang and F. Lu, “Insulated coupler structure design for the long-distance freshwater capacitive power transfer,” *IEEE Trans. Ind. Inform.*, vol. 16, no. 8, pp. 5191–5201, Aug. 2020.

[28] H. Zhang, F. Lu, H. Hofmann, W. Liu, and C. C. Mi, “A four-plate compact capacitive coupler design and LCL-compensated topology for capacitive power transfer in electric vehicle charging application,” *IEEE Trans. Power Electron.*, vol. 31, no. 12, pp. 8541–8551, Dec. 2016.

[29] E. Rong, P. Sun, K. Qiao, X. Zhang, G. Yang, and X. Wu, “Six-plate and hybrid-dielectric capacitive coupler for underwater wireless power transfer,” *IEEE Trans. Power Electron.*, vol. 39, no. 2, pp. 2867–2881, Feb. 2024.

[30] W. Zhou, Q. Gao, R. Mai, Z. He, and A. P. Hu, “Design and analysis of a CPT system with extendable pairs of electric field couplers,” *IEEE Trans. Power Electron.*, vol. 37, no. 6, pp. 7443–7455, Jun. 2022.

Ting Chen (Member, IEEE) received the B.S. degree in electrical engineering and automation, M.S. degree in control engineering, and Ph.D. degree in electrical engineering from the China University of Mining and Technology, Beijing, China, in 2015, 2017, and 2022, respectively.

From 2019 to 2021, she was a joint Ph.D. student with the Department of Electrical and Computer Engineering, San Diego State University, San Diego, CA, USA. She is currently an Associate Professor with the Department of Electrical Engineering, State Key Laboratory of Intelligent Power Distribution Equipment and System, Hebei University of Technology. Her current research interests include wireless power transfer technologies, modeling, and control of switching converters.

Yuqiao Wang received the B.S. degree in electrical engineering and automation in 2023 from the School of Electrical Engineering, Hebei University of Technology, Tianjin, China, where he is currently working toward the M.E. degree in electrical engineering.

His research interests include engineering electromagnetism, wireless power transfer, and its industrial applications.

Fengxian Wang received the B.S. degree in electrical engineering and the M.S. degree in electrical engineering from Tiangong University, Tianjin, China, in 2018 and 2021, respectively. He is currently working toward the Ph.D. degree in electrical engineering with the Hebei University of Technology, Tianjin, China.

His research interests include engineering electromagnetism, wireless power transfer, and its industrial applications.

Xian Zhang received the M.E. and Ph.D. degrees in electrical engineering from the Hebei University of Technology, Tianjin, China, in 2009 and 2012, respectively.

He is currently a Professor with the Hebei University of Technology, Tianjin, China. He is the Director of the China Electrotechnical Society and the secretary-general of the National Specialized Committee on Wireless Power Transmission Technology. His research interests include encompass intelligent high-power wireless power transmission technology, measurement of three-dimensional electromagnetic fields, and numerical calculations of modern engineering electromagnetic fields.

Xuan Zhao received the B.S. degree in electrical engineering and the M.S. degree in electrical engineering and automation in 2018 and 2022, respectively, from Hebei University of Technology, Tianjin, China, where he is currently working toward the Ph.D. degree in electrical engineering.

His research interests include engineering electromagnetism, wireless power transfer, and its industrial applications.

Guangyao Li received the B.S. degree in electronic engineering from the Tianjin Sino-German University of Applied Sciences, Tianjin, China, in 2022. He is currently working toward the M.E. degree in electrical engineering with the Hebei University of Technology, Tianjin, China.

His research interests include engineering electromagnetism, wireless power transfer, and its industrial applications.

Zhihui Ma received the B.S. degree in electrical engineering and automation from Shijiazhuang Tiedao University, Shijiazhuang, China, in 2021. He is currently working toward the M.E. degree in electrical engineering with the Hebei University of Technology, Tianjin, China.

His research interests include engineering electromagnetism, wireless power transfer, and its industrial applications.